A Distributed Analytical Electro-Thermal Model for Pouch-Type Lithium-Ion Batteries

Maryam Yazdanpour,[a,*] **Peyman Taheri,**[a] **Abraham Mansouri,**[b] **and Majid Bahrami**[a,**,z]

aLaboratory for Alternative Energy Conversion (LAEC), School of Mechatronic Systems Engineering, Simon Fraser University, Surrey, BC V3T 0A3, Canada
bDepartment of Mechanical Engineering, American University in Dubai, Dubai 28282, UAE

An analytic multi-physics model for pouch-type lithium-ion (Li-ion) batteries is presented. Both electrical and thermal processes are considered in the model to resolve their interplay on heat generation and battery thermal behavior. Voltage response of a sample Li-ion battery during galvanostatic discharge processes is measured to obtain a concentration-independent polarization expression. By numerically solving the charge balance equation on positive and negative electrodes in conjugation with the polarization expression, it is shown that the transfer current between the electrodes remains approximately constant, in particular when depth-of-discharge is less than 90%. Based on this observation, the electrochemical performance of the battery is simplified, and by using the method of separation of variables a closed-form electrical model is proposed. Joule heating on each electrode, calculated from the electrical model, is used as a local heat source in a two-dimensional battery thermal model. The distributed thermal model is solved analytically with the method of integral transform. The analytical results are successfully validated through comparisons with experimental and numerical data. It is confirmed that ohmic heating in the electrodes contributes to a relatively small portion (8-18%) of the total heat generation; nonetheless, since this heat is highly localized it results in spatial non-uniformity in temperature.
© 2014 The Electrochemical Society. [DOI: 10.1149/2.1191412jes] All rights reserved.

Lithium-ion (Li-ion) batteries are the systems of choice, offering high energy density, flexible and lightweight design, and longer lifespan than comparable battery technologies. Safety issues and cost (related to cycle and calendar life) that all are coupled to thermal effects in the batteries, are the main barriers to the development of large fleets of vehicles on public roads equipped with Li-ion cells.[1] Hence, the development and implementation of Li-ion batteries, particularly in automotive applications, requires substantial diagnostic and practical modeling efforts to fully understand the thermal characteristics in the batteries across various operating conditions.[2-4] Thermal modeling prompts the understanding of the battery thermal behavior beyond what is possible from experiments and it provides a basis for exploring thermal management strategies for batteries in hybrid electric vehicles (HEVs) and electric vehicles (EVs).[5]

In order to accurately predict the thermal response of Li-ion batteries, it is essential to evaluate the pattern and magnitude of heat generation and heat diffusion inside the electrochemical cell. This can be done through a physics-based thermo-electrochemical model;[6] nonetheless, such detailed electrochemical models are mostly recommended for cell design and optimization purposes due to their high fidelity, and they are not practical for real-time applications because of their high-order of complexity. Alternatively, when a battery exists and lab-generated data for the battery is available, empirical-based models which mimic the electrochemical performance of the battery can be developed. Indeed, simplicity and robustness of such models enables them to be applied in real-time embedded systems. Equivalent circuit models[7,8] and fitting function models[9] are common methodologies in this category. Kwon et al.[10] developed a fitting function model, originally proposed by Gu,[9] to construct a two-dimensional electrical model for Li-ion cells to predict the potential field and current density distributions in the positive and negative electrodes. Afterward, Kim et al.[11-13] presented a two-dimensional thermal model based on Kwon's model.[10] In Ref. 14, they extended their earlier thermal model to accommodate the dependence of the discharge behavior on the environmental temperature.

In all the above-mentioned studies, "numerical" approaches were adapted to solve the governing equations and obtain two-dimensional distributions of potential and current density on the electrodes along with the temperature field in the battery. This paper is the third in a series of planned works[15,16] in which the authors attempt to develop "analytical" tools for Li-ion battery simulations. In the present work,

superposition of electrochemical heat and Joulean heat is introduced in the irreversible portion of the heat generation term. The Joule heating contribution is evaluated by analytical description of the potential and current density fields. The contribution of the authors to the subject is development of a "linearly coupled" electro-thermal model for pouch-type Li-ion batteries. Although the proposed model is not as accurate as full physics-based models, it is computationally efficient and can be used as a fast simulation tool to predict the temperature distribution in pouch-type cells.

To analytically solve the balance equations for charge and energy in two-dimensional electrode domains, methods of separation of variables[16] and integral transform[15] are used, respectively. The results are compared to experimental and numerical data for standard constant current discharge tests with a fair agreement.

Formulation of the Problem

Figure 1a schematically shows the core of a pouch-type lithium-ion battery that is constructed of several cell assemblies, also known as electrode assemblies. In Fig. 1a,b single cell assembly is depicted. For better illustration, different layers in the cell assembly are shown separated while in the actual battery these layers are compressed; see Fig. 1b. Each cell assembly includes a negative electrode, two layers of separator sheets, and a positive electrode. The electrodes include active materials, required in the battery chemistry, coated on both sides of current collector foils. In most Li-ion batteries, the current collector in positive and negative electrodes are foils of aluminum and copper, respectively. The separator sheet is an electrically inert membrane for transportation of cations (Li+) between the electrodes. All layers, except current collectors, are porous and are soaked in a concentrated electrolyte liquid. The electrode tabs are the current collector foils extending outside the electrode plates for the purpose of electrical connection, and they are not covered by active materials.

Arrows in Fig. 1b present current streamlines during discharge processes. The through-plane straight arrows represent the transport of Li+ between the electrodes, i.e., transfer current. The in-plane arrows in *x*-*y* plane represent the transport of charges (e−), i.e., the electrical current, on the electrode layers. The direction of transfer and electric currents is reversed for a charging process. As shown in the Fig. 1b, electrical constriction occurs at the tabs of positive and negative electrodes. For the sake of convenience, the transfer current on both sides of each electrode can be considered to occur on one side of the electrodes. This approach is common in the literature.

*Electrochemical Society Student Member.
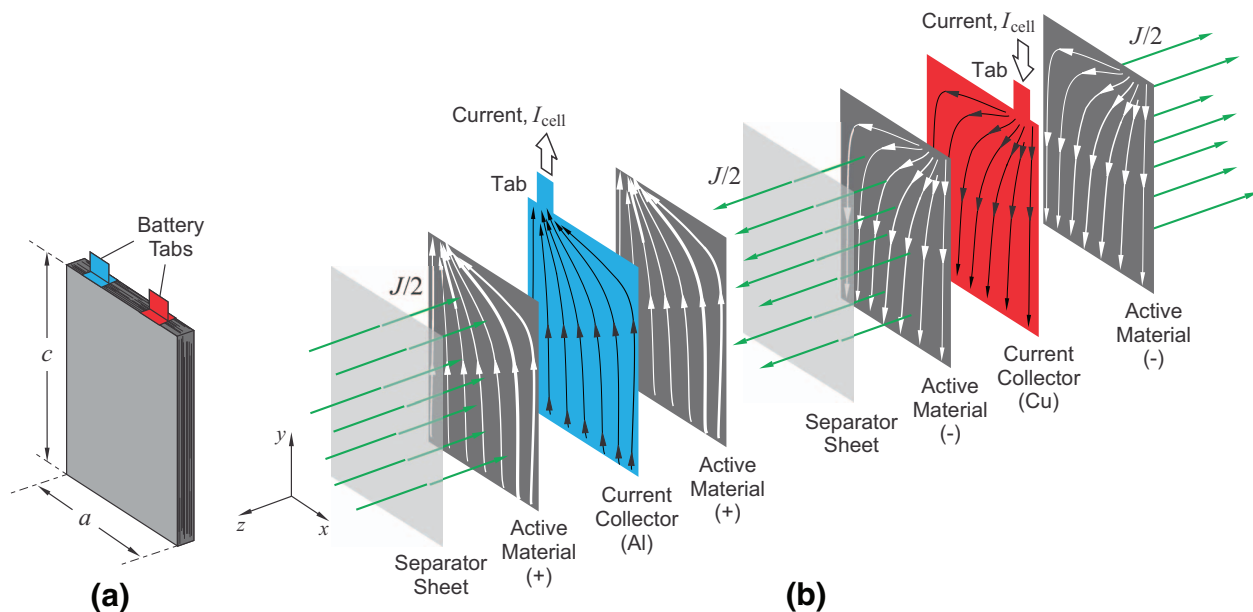**Electrochemical Society Active Member.
zE-mail: mbahrami@sfu.ca

Figure 1. a) Core (electrode-separator stack) of a pouch-type lithium-ion battery is shown. b) Schematic of a single cell assembly in the battery is shown. The battery core is constructed by repeating the cell assembly. Different layers of the cell are separated for the sake of presentation. The arrows in z-direction correspond to transfer current, the transport of Li^+ from the negative electrode to the positive electrode during a discharge process. The arrows in x-y plane represent current streamlines on electrodes.

Electrical model.— A dimensional analysis can be performed to show that owing to the small thickness of layers in the cell assembly, compared to their dimensions in x- and y-directions, the distribution of potential in the electrodes is two-dimensional in x-y plane.[17] Accordingly, the governing differential equation for the charge balance in each electrodes reads

$$-\nabla \cdot \mathbf{i}_j + \frac{\mathbf{J} \cdot \mathbf{n}_j}{\delta_{\text{elec},j}} = 0 \quad (j = p, n) \qquad [1]$$

where $\mathbf{i}_j = \{i_x, i_y, 0\}_j$ is the in-plane current density vector on each electrode (A m^{-2}). The subscript j corresponds to domains of the positive electrode Ω_p and the negative electrode Ω_n. The reaction current density vector on the electrodes is $\mathbf{J} = \{J_x, J_y, J\}$ in (A m^{-2}), where J_x and J_y are side reactions and are considered to be negligible. The through-plane component of the reaction current, J, referred to as transfer current, corresponds to the intercalation of lithium ions in active materials on both sides of the electrodes. The electrode thickness in z-direction is $\delta_{\text{elec},j}$ in (m), and $\mathbf{n}_j$ is the unit normal vector on each electrode surface pointing outward; $\mathbf{n}_p = \{0, 0, -1\}$ and $\mathbf{n}_n = \{0, 0, +1\}$.

According to the Ohm's law, components of $\mathbf{i}_j$ are related to the potential distribution via

$$i_{x,j} = -\sigma_{\text{eff},j}\frac{\partial V_j}{\partial x} \quad \text{and} \quad i_{y,j} = -\sigma_{\text{eff},j}\frac{\partial V_j}{\partial y} \quad (j = p, n) \quad [2]$$

where x and y indicate the spatial position (m), and $V_j = V_j(x, y)$ is the two-dimensional potential distribution in the electrode (V).

The quantity $\sigma_{\text{eff},j}$ is the effective electrical conductivity (S m^{-1}), that for each electrode is

$$\sigma_{\text{eff},j} = \frac{1}{\delta_{\text{elec},j}}(\delta_{\text{cc},j}\,\sigma_{\text{cc},j} + 2\delta_{\text{am},j}\,\sigma_{\text{am},j}) \quad (j = p, n)$$

where

$$\delta_{\text{elec},j} = \delta_{\text{cc},j} + 2\delta_{\text{am},j} \quad (j = p, n)$$

$\delta_{\text{cc},j}$ and $\delta_{\text{am},j}$ are thicknesses of current collector and active material layers, respectively. Electrical conductivity of the current collector and the active material are denoted by $\sigma_{\text{cc},j}$ and $\sigma_{\text{am},j}$.

As depicted in Fig. 2, each electrode can be considered as a rectangular domain in x-y plane of width a and height c. The through-plane

current enters (or exits) the domain through its surface in x-y plane, whereas the in-plane current is allowed to exit (or enter) the domain through the tab constriction of width b on the boundary at $y = c$. The distance between the center of the tab and y-axis is denoted by e_j.

It is important to mention that unlike Refs. [3 and 17] geometry of the tabs are not included in our analysis, since the proposed analytical solutions cannot be obtained if the tabs were included in the calculation domain, due to complexity of the geometry.

With reference to Fig. 2, the relevant boundary conditions for Eq. (1) at the positive domain are

$$-\sigma_{\text{eff},p}\frac{\partial V_p}{\partial x} = 0 \quad \text{at} \quad x = 0 \qquad [3a]$$

$$-\sigma_{\text{eff},p}\frac{\partial V_p}{\partial x} = 0 \quad \text{at} \quad x = a \qquad [3b]$$

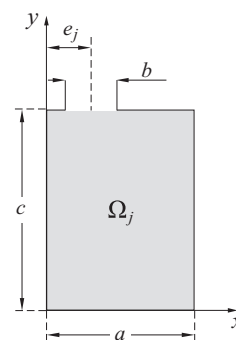$$-\sigma_{\text{eff},p}\frac{\partial V_p}{\partial y} = 0 \quad \text{at} \quad y = 0 \qquad [3c]$$

Figure 2. Two-dimensional schematic of electrodes in x-y plane. Width and height of electrodes and width of the electrode tab are the same for both positive and negative electrodes. The distance of the tab center from y-axis, denoted by e_j, differs between the electrodes.

$$-\sigma_{\text{eff},p}\frac{\partial V_p}{\partial y} = i_{\text{tab},p} \quad \text{at} \quad e_p - \frac{b}{2} < x < e_p + \frac{b}{2}, \quad y = c \quad [3d]$$

$$-\sigma_{\text{eff},p}\frac{\partial V_p}{\partial y} = 0 \quad \text{at} \quad e_p + \frac{b}{2} < x < e_p - \frac{b}{2}, \quad y = c \quad [3e]$$

Similarly, for the negative domain

$$-\sigma_{\text{eff},n}\frac{\partial V_n}{\partial x} = 0 \quad \text{at} \quad x = 0 \quad [4a]$$

$$-\sigma_{\text{eff},n}\frac{\partial V_n}{\partial x} = 0 \quad \text{at} \quad x = a \quad [4b]$$

$$-\sigma_{\text{eff},n}\frac{\partial V_n}{\partial y} = 0 \quad \text{at} \quad y = 0 \quad [4c]$$

$$V_n = 0 \quad \text{at} \quad e_n - \frac{b}{2} < x < e_n + \frac{b}{2}, \quad y = c \quad [4d]$$

$$-\sigma_{\text{eff},n}\frac{\partial V_n}{\partial y} = 0 \quad \text{at} \quad e_n + \frac{b}{2} < x < e_n - \frac{b}{2}, \quad y = c \quad [4e]$$

The above boundary conditions imply that no current passes through boundaries of Ω_p and Ω_n except for the tab boundaries. In Eq. (3d), $i_{\text{tab},p}$ is the in-plane current density (A m^{-2}) at the tab of positive electrode

$$i_{\text{tab},p} = \frac{I_{\text{cell}}}{b\,\delta_{\text{elec},p}} \quad [5]$$

where I_{cell} is the applied discharge current (A) for a single cell (electrode) assembly, and $b\,\delta_{\text{elec},p}$ is the cross-sectional area of the positive tab. In Eq. (4d), potential at the tab boundary of the negative electrode is set to zero in order to provide a reference for voltage distribution.[18] The electrical model is based on charge balance equation (current continuity), thus the current which enters one electrode should leave the other one. The boundary conditions at the tabs can be given for either current density or potential. In Eq. (3d) boundary condition for current density is given, while in Eq. (4d) boundary condition for potential is provided.

Thermal model.— In the electrical model it was assumed that potential distribution is independent of z-direction. This assumption can be extended to the thermal model as well; since thickness of electrodes in z-direction is very small compared to their dimensions in x- and y-directions, heat will conduct quickly across the thin direction and the temperature will become, to a good approximation, uniform across z-direction.[19]

For battery assemblies which include a stack of electrodes, a three-dimensional thermal model is preferred for accurate thermal analysis; however, our previous 3D simulations[15] for the considered battery showed small variations of temperature in z-direction, particularly at low values of convective heat transfer coefficient. Accordingly, in this study a two-dimensional thermal model is proposed for thin electrodes and it is extended for the whole electrode stack.

The transient temperature field in the cell assembly is described by a two-dimensional energy equation

$$-\nabla \cdot \mathbf{q} + \dot{g} = \rho c_p \frac{\partial T}{\partial t} \quad [6]$$

where $\mathbf{q} = \{q_x, q_y, 0\}$ is the in-plane heat flux vector on each electrode (W m^{-2}), $\dot{g}$ is the net rate of volumetric heating inside the battery (W m^{-3}), ρ is the density of cell assembly (kg m^{-3}), c_p is its specific heat capacity (J kg^{-1} K^{-1}), t is the time (s), and $T = T(x, y)$ is the two-dimensional temperature distribution in the cell (K).

According to the Fourier's law for heat conduction, components of $\mathbf{q}$ are related to the temperature distribution via

$$q_x = -\kappa_{\text{eff}}\frac{\partial T}{\partial x} \quad \text{and} \quad q_y = -\kappa_{\text{eff}}\frac{\partial T}{\partial y} \quad [7]$$

The quantity κ_{eff} is the effective in-plane thermal conductivity of the cell assembly (W m^{-1} K^{-1}), calculated from

$$\kappa_{\text{eff}} = \frac{1}{\delta_{\text{cell}}}(\delta_{cc,p}\,\kappa_{cc,p} + \delta_{cc,n}\,\kappa_{cc,n} + 2\delta_{\text{am},p}\,\kappa_{\text{am},p} + 2\delta_{\text{am},n}\,\kappa_{\text{am},n} + 2\delta_{ss}\,\kappa_{ss})$$

where

$$\delta_{\text{cell}} = \delta_{cc,p} + \delta_{cc,n} + 2\delta_{\text{am},p} + 2\delta_{\text{am},n} + 2\delta_{ss}$$

with δ_{ss} as the thickness of separator sheet. Thermal conductivities of current collector foils, active materials, and separator sheet are denoted by κ_{cc}, κ_{am}, and κ_{ss}, respectively.

The net rate of volumetric heating inside the battery is the difference between heat generation and heat dissipation rates

$$\dot{g} = \nu_{ec}\,\dot{g}_{ec} + \nu_{\text{elec},p}\,\dot{g}_{\text{ohm},p} + \nu_{\text{elec},n}\,\dot{g}_{\text{ohm},n} - \frac{q_{\text{diss}}}{\delta_{\text{cell}}} \quad [8]$$

where $\dot{g}_{ec}$ and $\dot{g}_{\text{ohm},j}$ are the electrochemical and ohmic heat generation rates per unit volume. The coefficients ν_{ec} and $\nu_{\text{elec},j}$ are volume ratios for electrochemical and ohmic heat generation rates[17]

$$\nu_{ec} = \frac{\mathcal{V}_{ec}}{\mathcal{V}_{\text{cell}}} = \frac{2\delta_{\text{am},p} + 2\delta_{\text{am},n} + 2\delta_{ss}}{\delta_{\text{cell}}}$$

$$\nu_{\text{elec},j} = \frac{\mathcal{V}_{\text{elec},j}}{\mathcal{V}_{\text{cell}}} = \frac{2\delta_{\text{am},j} + 2\delta_{cc,j}}{\delta_{\text{cell}}} \quad (j = p, n)$$

The quantities $\mathcal{V}_{\text{cell}}$, $\mathcal{V}_{\text{elec},j}$, and $\mathcal{V}_{ec}$ denote the total volume of the cell assembly, volume of each electrode, and volume of the cell which participates in electrochemical reactions.

Worth mentioning that, since electrochemical processes include migration and diffusion of charges between the electrodes through the electrolyte (separator) and intercalation reaction in active materials, the separator sheet is part of the electrochemical cell and must be included in ν_{ec} as discussed in Ref. 17.

The electrochemical heat in each electrode is calculated from[21]

$$\dot{g}_{ec} = \frac{I_{\text{cell}}}{\mathcal{V}_{\text{cell}}}\left[(V_p - V_n) - V_{oc} + T\frac{dV_{oc}}{dT}\right] \quad [9]$$

where I_{cell} is positive/negative for charge/discharge processes. The last term in Eq. (9) is the reversible heat of electrochemical reactions, while the rest is the irreversible heat due to the cell overpotential. In this study, we assume that open circuit voltage V_{oc} linearly depends on temperature, that is, dV_{oc}/dT is constant and its value is considered 0.0002 (V K^{-1}).[22,23]

For each electrode, the ohmic (Joulean) heat generation rate reads

$$\dot{g}_{\text{ohm},j} = \frac{1}{\sigma_{\text{eff},j}}\left(i_{x,j}^2 + i_{y,j}^2\right) \quad (j = p, n) \quad [10]$$

where i_x and i_y are the components of in-plane current density on each electrode obtained from the electrical model; see Eq. (2).

The last term in Eq. (8) takes account for the volumetric heat dissipation to the ambient from x-y plane. The heat dissipation flux q_{diss} is calculated from Newton's law of cooling

$$q_{\text{diss}} = 2h_{\text{eff}}(T_s - T_0) \quad [11]$$

where T_0 is the constant ambient temperature, T_s is the surface temperate, and h_{eff} is the effective heat transfer coefficient (W m^{-2} K^{-1}) at the surface of the cell (both front and back surfaces in x-y plane).

The thermal boundary conditions for the energy balance equation [cf. Eq. (6)] are

$$-\kappa_{\text{eff}}\frac{\partial T}{\partial x} = \left[\frac{\delta_{\text{case}}}{\kappa_{\text{case}}} + \frac{1}{h_{x,0}}\right]^{-1}(T - T_0) \quad \text{at} \quad x = 0 \quad [12a]$$

$$+\kappa_{\text{eff}}\frac{\partial T}{\partial x} = \left[\frac{\delta_{\text{case}}}{\kappa_{\text{case}}} + \frac{1}{h_{x,a}}\right]^{-1}(T - T_0) \quad \text{at} \quad x = a \quad [12b]$$

$$-\kappa_{\text{eff}}\frac{\partial T}{\partial y} = \left[\frac{\delta_{\text{case}}}{\kappa_{\text{case}}} + \frac{1}{h_{y,0}}\right]^{-1}(T - T_0) \quad \text{at} \quad y = 0 \qquad [12c]$$

$$+\kappa_{\text{eff}}\frac{\partial T}{\partial y} = \left[\frac{\delta_{\text{case}}}{\kappa_{\text{case}}} + \frac{1}{h_{y,c}}\right]^{-1}(T - T_0) \quad \text{at} \quad y = c \qquad [12d]$$

where δ_{case} and κ_{case} are the thickness and the thermal conductivity of the battery case, respectively; see Table II. The convective heat transfer coefficients are denoted by h (W m^{-2} K^{-1}) with relevant subscripts which indicate the location of the boundary.

The initial temperature of the battery is assumed to be the ambient temperature

$$T = T_0 \quad \text{at} \quad t = 0 \qquad [13]$$

Experimental

Experimental battery.— For experimentation, we use a 20 Ah pouch-type Li-ion battery (EiG Battery, South Korea). An image from the layered structure of the battery core, i.e., electrode-separator stack, is depicted in Fig. 3a. Lithiated nickel-manganese-cobalt (NMC) oxides and lithiated graphite are used as active materials at positive and negative electrodes, respectively. In Fig. 3b, laminated structure of a negative electrode is shown; a layer of active material coated on both sides of a copper foil (one side is shown); compare with Fig. 1.

The experimental battery includes 18 cell assemblies connected in parallel, with a z-fold design for the separator sheet. For parallel connection of the cells, electrode tabs of the same type are welded
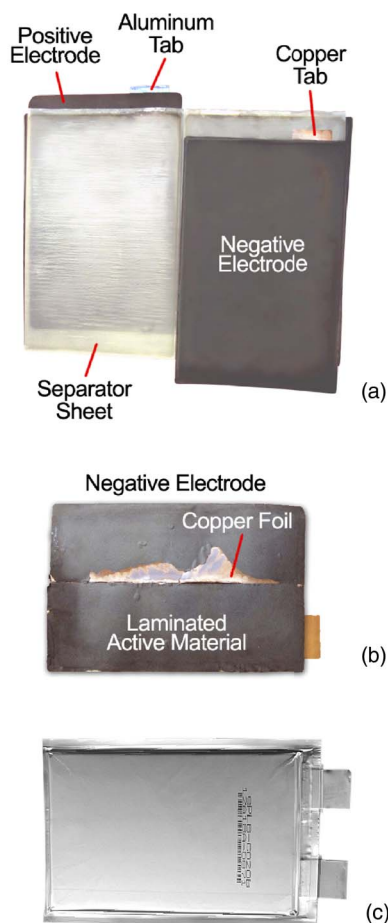

Figure 3. a) Core structure of the experimental battery. b) Layered structure of a negative electrode. c) The actual experimental battery with the pouch case.

Table I. Dimensions of electrode domains Ω_p and Ω_n in x-y plane, corresponding to Fig. 2.

Electrode	a (m)	b (m)	c (m)	e (m)
Positive	125×10^{-3}	30×10^{-3}	195×10^{-3}	27×10^{-3}
Negative	125×10^{-3}	30×10^{-3}	195×10^{-3}	98×10^{-3}

together to form the battery terminals. The electrode-separator stack is soaked in an organic electrolyte solution and packed in a pouch case with terminals extending outside the pouch, see Fig. 3c. A mixture of ethylene carbonate (EC) and diethyl carbonate (DEC) are the solvents and LiPF$_6$ is the solute for the electrolyte.

With reference to Fig. 2, electrode dimensions in x-y plane are listed in Table I. The thickness, thermal conductivity, and electrical conductivity of the battery components (layers) are given in Table II.

Voltage response of the battery V_{batt} during discharge processes at various C-rates (0.5C, 1C, 2C, 3C and 4C) is measured at the constant environmental temperature of $T_0 = 22°$C, see Fig. 4. During discharge processes, the battery was subjected to natural convection cooling. Because of the excessive temperature rise (above the safety limit) in the battery during 4C-rate discharge, the voltage measurement is terminated before completion of the process.

Experimental system.— A power processing unit (ABC-150, AeroVironment, USA) was used to charge and discharge the battery. Charge and discharge protocols were scripted in Emerald software (Greenlight Innovation, Canada) to control the power processing unit. A PC, connected to the power processing unit through a controller area network (CAN) connection, was used for software-hardware communication and for data collection. Five T-type thermocouples with the accuracy of $\pm0.5°$C were attached to the battery surface, two at the vicinity of the tabs, one at the center, and two at the bottom corners. Voltage at the battery tabs (terminals) and temperature at different locations were collected through a data acquisition (DAQ) system (Greenlight Innovation, Canada) every 10 seconds.

Before every discharge test, Constant Current-Constant Voltage protocol (20 A, 4.15 V max with 2 A cutoff) was used to fully charge the battery at the room temperature of 22°C. For equilibrium voltage and temperature to be established, the fully charged batteries were allowed to rest for at least six hours before a discharging test begins.

Specific heat measurement.— The specific heat capacity c_p, of the experimental battery as a function of temperature was measured over a temperature range of 298–323 K. The measurement was performed with an accelerated rate calorimeter (ARC) (Thermal Hazard Technology, UK) with a heat detection sensitivity at 0.02 K min^{-1}. In Fig. 5, samples of measured value for specific heat with respect to temperature are shown. Dependency of c_p on T is approximated by a quadratic polynomial fit

$$c_p(T) = -81481.2 + 518.523\,T - 0.811504\,T^2 \qquad [14]$$

The above correlation is used for numerical simulations, and an average value of 1250 (J kg^{-1} K^{-1}) is considered in the analytical model.

Polarization Expression

Distribution of the transfer current density J, which appears in the electrical model [cf. Eq. (1)], is dictated by the local rate of electrochemical reactions in electrodes. For an accurate description of J a distributed electrochemical model[5,17] is preferred. In this study, instead of using an electrochemical model, a mathematical model[24,9] is employed to predict the time dependent distribution of J in the experimental battery during constant-current discharge processes. The model uses a concentration-independent polarization expressions to describe the local overpotential between the electrodes. Some parameters in the polarization expression must be evaluated from experi-

Table II. Thickness, thermal conductivity, and electrical conductivity of battery components.[15]

Material/Layer	Thickness, δ (m)	Thermal conductivity, κ (W m^{-1} K^{-1})	Electrical conductivity, σ (S m^{-1})
Aluminum current collector	21×10^{-6}	238	37.8×10^{6}
Copper current collector	12×10^{-6}	398	59.6×10^{6}
Separator sheet	25×10^{-6}	0.34 (wet)	-
Positive active material	70×10^{-6}	1.58 (wet)	13.9 (wet)
Negative active material	79×10^{-6}	1.04 (wet)	100 (wet)
Pouch (case)	162×10^{-6}	0.16	-

mental data. The procedure explained below can be applied to obtain polarization expressions for both charge and discharge processes. For charge processes, experimental data for charging are required. In this study, only discharge mode is considered.

Experimental observations[9] and electrochemical simulations[25] of galvanostatic discharge processes confirm that at a fixed depth-of-discharge (DOD), the battery voltage exhibits an approximately linear dependency on the current density. Accordingly, a linear polarization expression can be assumed as[18,24,9]

$$J(x, y) = Y_{ec}[V_p(x, y) - V_n(x, y) - V_{oc}] \quad [15]$$

where, Y_{ec} is the electrochemical conductance (i.e., the conductance of separator and electrolyte) per unit area of the cell (S m^{-2}), and $V_p - V_n$ corresponds to the potential difference between two points on the positive and negative electrodes with the same coordinates in x-y plane. By convention, J assumes positive and negative values for charge and discharge processes, respectively.
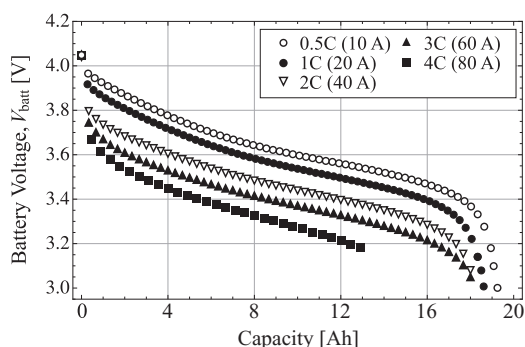

Figure 4. Measured voltage response of the battery during constant-current discharge processes at different discharge rates at environmental temperature of 22°C.
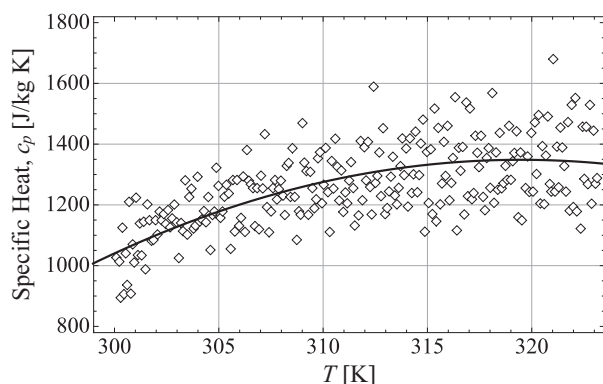

Figure 5. Dependency of specific heat capacity c_p on temperature. A quadratic polynomial (line) is fitted to experimental data (symbols).

The current of the cell assembly I_{cell} and the current of battery I_{batt} are related to the transfer current density J via

$$I_{cell} = \int_0^a \int_0^c J(x, y) \, dy \, dx \quad \text{and} \quad I_{batt} = I_{cell} N \quad [16]$$

The number of cell assemblies inside the battery core [cf. Fig. 1a] is denoted by N. For the considered battery $N = 18$.

In the mathematical model, both Y_{ec} and V_{oc} are considered to solely depend on DOD, and their dependency is expressed in a polynomial form

$$Y_{ec} = \sum_{l=0}^{L} \mathscr{C}_l \, \text{DOD}^l \quad [17]$$

$$V_{oc} = \sum_{m=0}^{M} \mathscr{D}_m \, \text{DOD}^m \quad [18]$$

where $\mathscr{C}_l$ and $\mathscr{D}_m$ are the constants to be determined from experimental voltage data during constant-current discharge processes.

DOD is defined as the fraction of cell capacity Q_{cell} (Ah), released during a discharge process. Given an initial DOD at $t = 0$ and assuming 100% coulombic efficiency, DOD (in %) can be calculated related to discharge time t (s) via

$$\text{DOD}(t) = \text{DOD}(0) + \frac{1}{3600 \, Q_{cell}} \int_0^t |I_{cell}(t)| \, dt \quad [19]$$

where $Q_{cell} = Q_{batt}/N$ and the constant 3600 has the unit of second/hour.

To find coefficients $\mathscr{C}_l$ and $\mathscr{D}_m$, experimental data must be used to evaluate the battery voltage V_{batt}, at different DOD values during discharge processes at different currents. In Fig. 6, battery voltage
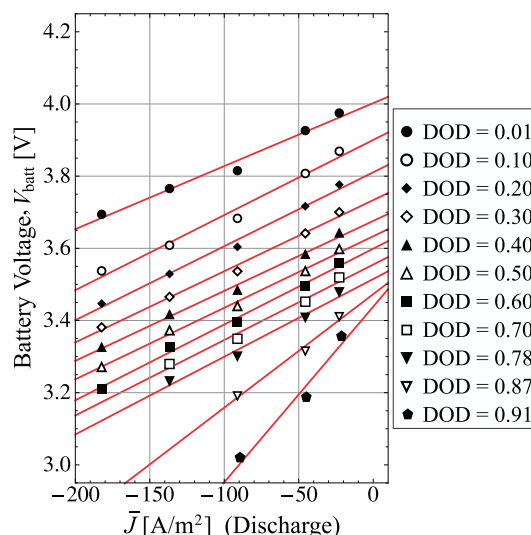

Figure 6. The linear dependency of battery voltage and transfer current density at constant values of DOD.
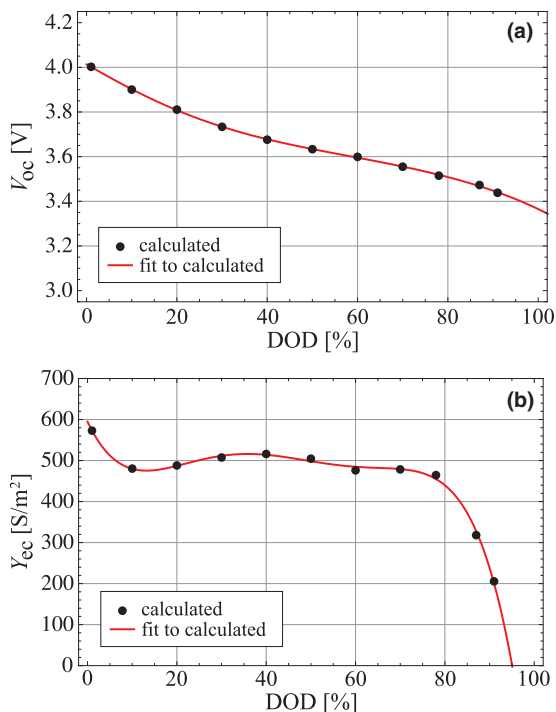
Figure 7. a) The dependency of open-circuit potential V_{oc} on DOD. b) The dependency of electrochemical conductance Y_{ec} on DOD.

variations are plotted against mean value for the transfer current $\bar{J}$

$$\bar{J} = \frac{I_{cell}}{a\,c} \quad [20]$$

The mean transfer current $\bar{J}$ only varies with the applied current, and during a constant current charge/discharge it remains constant and independent to DOD. However, based on Eq. (17) and (18), V_{oc} and Y_{ec} are functions of DOD, thus, distribution of J depends on DOD as given in Eq. (15).

As shown in the figure, at a constant DOD, variations of the battery voltage versus transfer current density, shown by symbols, can be approximated by a linear function (lines). In account for Eq. (15), Y_{ec} is the inverse of the line slope and V_{oc} is the intercept.[9]

Plots in Fig. 7a and b depict the dependency of V_{oc} and Y_{ec} on DOD, obtained from measurements [cf. Fig. 4] and the above-mentioned procedure. Solid lines present sixth-order polynomial fits to the calculated values (symbols). The coefficients $\mathscr{C}_l$ and $\mathscr{D}_m$ for these polynomials are listed in Table III.

To account for temperature effects in the polarization expression, dependency of the electrochemical conductance and open-circuit potential on temperature must be considered. According to Arrhenius equation which gives the relationship between the electrochemical reaction rate constant and the temperature, a temperature dependent

Table III. Coefficients for Y_{ec} and V_{oc} polynomials in Eqs. (17) and (18).

$\mathscr{C}_l$	Value (S m^{-2})	$\mathscr{D}_m$	Value (V)
$\mathscr{C}_0$	594.8194516757329	$\mathscr{D}_0$	4.013429415861242
$\mathscr{C}_1$	−2314.500611172978	$\mathscr{D}_1$	−1.1609049213087084
$\mathscr{C}_2$	15185.333734108322	$\mathscr{D}_2$	0.21735802935895338
$\mathscr{C}_3$	−39468.79062965648	$\mathscr{D}_3$	3.3143732685737533
$\mathscr{C}_4$	42136.30840773217	$\mathscr{D}_4$	−6.186763856880206
$\mathscr{C}_5$	−11356.469694644662	$\mathscr{D}_5$	4.447106419266555
$\mathscr{C}_6$	−5156.616059847135	$\mathscr{D}_6$	−1.2793151751457248

Y_{ec} can be defined[26,27]

$$Y_{ec} = Y_{ec,ref}\,\mathrm{Exp}\left[\mathscr{C}_T\left(\frac{1}{T}-\frac{1}{T_{ref}}\right)\right] \quad [21]$$

Furthermore, Nernst equation which gives the relationship between the equilibrium potential and the temperature can be used to describe the Seebeck effect on V_{oc}[26,27]

$$V_{oc} = V_{oc,ref} + \mathscr{D}_T\,(T - T_{ref}) \quad [22]$$

The coefficients $\mathscr{C}_T$ and $\mathscr{D}_T$ are constants that must be determined from several sets of experiments at different environmental temperatures[26,27] to fit the temperature dependency of Y_{ec} and V_{oc}. The subscript 'ref' denotes values at a reference temperature T_{ref}. In this study, $T = T_{ref}$ is considered, where $T_{ref} = 22°C$.

Numerical Analysis

Equations in Formulation of the Problem and Polarization Expression Sections which govern the electro-thermal performance of the cell, form a nonlinear system and must be solved numerically. A finite element PDE solver, COMSOL MULTIPHYSICS (Version 4.3a), is used to simultaneously solve the governing equations over two separated domains, Ω_p and Ω_n, to obtain: i) the transient fields of potential on each electrode, ii) variations of transfer current density between the electrodes, and iii) temperature distribution in the cell assembly.

Once the potential distribution on positive and negative electrodes is calculated numerically, averaged potential over the positive tab at different DOD values yields the voltage response of the battery

$$V_{batt} = V_{tab,p} - V_{tab,n} = \frac{1}{b}\int_{e_p-\frac{b}{2}}^{e_p+\frac{b}{2}} V_p\,(x,c)\,dx \quad [23]$$

where b is the width of the tab.

In Fig. 8, voltage response of the battery at different discharge rates, calculated from Eq. (23), is compared to experimental voltage values, i.e., data in Fig. 4. The comparison shows a satisfactory agreement between the calculated and measured voltage of the battery, even at the nonlinear portion of discharge curves. Note that since cell assemblies inside the battery core are connected in parallel, $V_{batt} = V_{cell}$.

Our numerical analysis shows that at the beginning of a discharge process, the transfer current density J is concentrated near the tabs. At mid-way through the discharge the distribution of J becomes quite uniform, but still remains slightly higher in the vicinity of tabs. However, near the end of discharge when active materials are depleted near the tabs, the transfer current is forced away from the tabs toward the bottom of electrodes where active materials are less utilized. We observed this trend at all discharge rates.

To investigate the distribution of transfer current density during discharge processes, its maximum and minimum values are reported relative to the mean value and normalized by the mean value, i.e.,
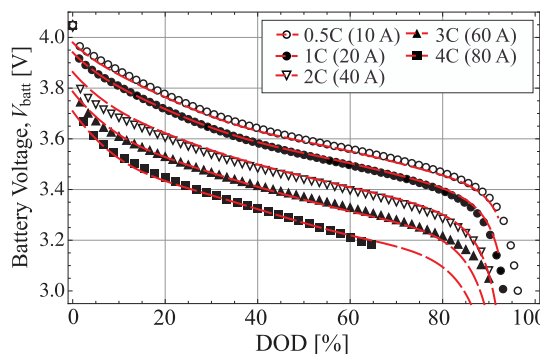

Figure 8. Variation of the battery voltage versus depth-of-discharge (DOD) for different discharge currents is shown. Symbols correspond to measured values and lines represent numerically calculated values.
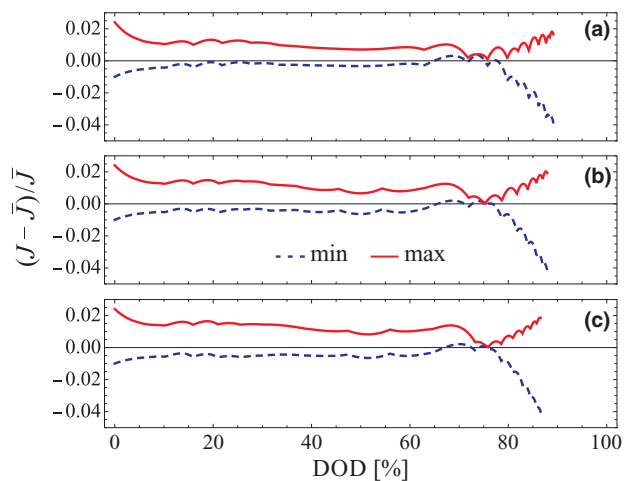
Figure 9. Minimum and maximum deviations of transfer current density J with respect to the mean value $\bar{J}$ are shown during discharge processes at 2C-rate (plot a), 3C-rate (plot b), and 4C-rate (plot c).

$(J - \bar{J})/\bar{J}$. Variation of $(J_{\min} - \bar{J})/\bar{J}$ and $(J_{\max} - \bar{J})/\bar{J}$ with respect to DOD at different discharge rates (2C, 3C, and 4C) are calculated from numerical model and plotted in Fig. 9. The plots confirm that maximum deviation of J with respect to $\bar{J}$ is about 6%. This observation suggests that a uniform transfer current can be assumed during discharge processes. This is the key assumption in development of the analytical electro-thermal model in the following sections.

Analytical Solutions

In this section, closed-form analytical solutions for electrical problem Electrical Model Section and thermal problem Electrical Model Section are developed. We shall solve the electrical problem first to find the distribution of in-plane current density vector $\mathbf{i}_j$ on electrodes. Nonetheless, in order to approach the problem analytically, a uniform transfer current density J must be assumed.

Results from the numerical analysis show that transfer current is not uniformly distributed; however, its variation is not drastic—less then 6% during most of the discharge process, as shown in Fig. 9. Accordingly, a uniform transfer current density is superimposed in our analysis which allows to develop a theoretical electro-thermal analysis. A similar assumption is proposed by Doyle and Newman[20] for development of an analytical electrochemical model. Note that, the uniformity of transfer current density is a desired feature for Li-ion batteries; it means that active materials are evenly utilized and battery degradation rate is minimized.

The assumptions made in deriving the analytical electro-thermal model are as follow:

- uniform distribution of transfer current density [cf. Eq. (20)],
- uniform current density at the battery tabs [cf. Eq. (5)],
- potential and temperature distributions are independent of z-direction,
- electrical and thermal conductivities, density, and heat capacity are independent of temperature,
- constant convection heat transfer coefficient and ambient temperature.

Analytical solution for potential and current density distributions.— The solution for Eq. (1) can be obtained by a simple transformation followed by the method of separation of variables; for detailed calculations see Refs. 16 and 28. The two-dimensional distribution of potential on each electrodes ($j = p, n$)

can be described as

$$V_j(x, y) = -\frac{1}{2} \frac{\bar{\mathbf{J}} \cdot \mathbf{n}_j}{\delta_{\text{elec}, j} \, \sigma_{\text{eff}, j}} y^2 + \sum_{k=1}^{\infty} A_{k,j} \cos(\alpha_k x) \cosh(\alpha_k y) \quad [24]$$

in which the summation is taken over all discrete spectrum of eigenvalues $\alpha_k = k\pi/a$. The terms $\cos(\alpha_k x)$ and $\cosh(\alpha_k y)$ are the eigenfunctions, and $A_{k,j}$ is a coefficient determined from electrical boundary conditions for each electrode and the orthogonality condition for eigenfunctions[28]

$$A_{k,j} = \frac{4(\bar{\mathbf{J}} \cdot \mathbf{n}_j) c [b \sin(\alpha_k a) - 2a \sin(\alpha_k b/2) \cos(\alpha_k e_j)]}{\delta_{\text{elec}, j} \, \sigma_{\text{eff}, j} \, b \, \alpha_k \sinh(\alpha_k c) [2\alpha_k a + \sin(2\alpha_k a)]} \quad [25]$$

The components of in-plane current density vector on each electrode can be obtained from Eq. (2) using the potential solution in (24).

Analytical solution for temperature distribution.— Equation (6) that describes the transient temperature distribution inside the battery core is solved analytically using the method of integral-transform. Details of the method implementation to batteries are discussed in Refs. [28–30].

Using the polarization expression in Eq. (15), one can rewrite the overpotential term in Eq. (9) as

$$V_p - V_n - V_{\text{oc}} = \frac{\bar{J}}{Y_{\text{ec}}} \quad [26]$$

Accordingly, the electrochemical heat generation in Eq. (9) recasts to

$$\dot{g}_{\text{ec}} = \frac{I_{\text{cell}}}{\mathcal{V}_{\text{cell}}} \left[\frac{\bar{J}}{Y_{\text{ec}}} + T \frac{dV_{\text{oc}}}{dT} \right] \quad [27]$$

For the sake of convenience in formulation of the integral-transformation technique we define a new temperature function $\theta(x, y, t) = T(x, y, t) - T_0$. The respective double integral-transformation and the inversion formula for $\theta(x, y, t)$ in a two-dimensional domain with $x \in [0, a]$ and $y \in [0, c]$ are

$$\bar{\bar{\theta}}(\beta_m, \gamma_n, t) = \int_{x'=0}^{a} \int_{y'=0}^{c} \Phi(\beta_m, x') \cdot \Psi(\gamma_n, y') \cdot \theta(x', y', t) \cdot dx' \cdot dy'$$

$$[28a]$$

$$\theta(x, y, t) = \sum_{m=1}^{\infty} \sum_{n=1}^{\infty} \Phi(\beta_m, x) \cdot \Psi(\gamma_n, y) \cdot \bar{\bar{\theta}}(\beta_m, \gamma_n, t) \quad [28b]$$

where the functions $\Phi(\beta_m, x)$ and $\Psi(\gamma_n, y)$ are the transformation kernels (normalized eigenfunctions); β_m and γ_n denote infinite lists of eigenvalues in x- and y-directions, respectively.

For two common thermal boundary conditions, i.e., convective cooling with a finite heat transfer coefficient h and adiabatic condition with $h = 0$, the kernels and the eigenvalues are given in Table IV. In the table, kernels and eigenvalues for an indicative direction (x-direction) are presented. To find the kernels and eigenvalues in y-direction, one needs to modify the relations for the boundary conditions at y-direction between the boundaries at $y = 0$ and $y = c$; for more details see Ref. 31.

By applying the method of integral transform, partial differential equation of energy [cf. Eq. (6)] can be transformed into an ordinary differential equation with the following analytical solution

$$T(x, y, t) = T_0 + \sum_{m=1}^{\infty} \sum_{n=1}^{\infty} \Phi(\beta_m, y) \cdot \Psi(\gamma_n, x) \cdot \exp\left(-\frac{\Delta_{m,n}}{\rho c_p} t\right)$$

$$\times \left[\int_t \frac{\bar{\bar{g}}(t)}{\rho c_p} \exp\left(\frac{\Delta_{m,n}}{\rho c_p} t\right) dt + C \right] \quad [29]$$

where

$$\Delta_{m,n} = v_{\text{ec}} \frac{I_{\text{cell}}}{\mathcal{V}_{\text{cell}}} \frac{dV_{\text{oc}}}{dT} + \kappa_{\text{eff}} \left(\lambda_n^2 + \lambda_m^2\right) \quad [30]$$

Table IV. The transformation kernels and the eigenvalues for use in integral transform (Fourier transform) and inversion formula in Eq. (28) for a finite region, $0 \leq x \leq a$.

Boundary condition at $x = 0$	Boundary condition at $x = a$	Kernel $\Phi(\beta_m, x)$	Eigenvalues β_m's are positive roots of
$H_{x,0} = \dfrac{h_{x,0}}{\kappa_{\text{eff}}} = $ finite	$H_{x,a} = \dfrac{h_{x,a}}{\kappa_{\text{eff}}} = $ finite	$\dfrac{\sqrt{2}\,[\beta_m \cos(\beta_m x) + H_{x,0} \sin(\beta_m x)]}{\left[\left(\beta_m^2 + H_{x,0}^2\right)\left(a + \dfrac{H_{x,a}}{\beta_m^2 + H_{x,a}^2}\right) + H_{x,0}\right]^{1/2}}$	$\tan(\beta a) = \dfrac{\beta(H_{x,0} + H_{x,a})}{\beta^2 - H_{x,0} H_{x,a}}$
$H_{x,0} = \dfrac{h_{x,0}}{\kappa_{\text{eff}}} = 0$	$H_{x,a} = \dfrac{h_{x,a}}{\kappa_{\text{eff}}} = 0$	$\sqrt{\dfrac{2}{a}}\,\cos(\beta_m x)^{\text{a}}$	$\sin(\beta a) = 0$

[a] Replace $\sqrt{2/a}$ by $\sqrt{1/a}$ for $\beta = 0$.

$$\bar{\bar{g}} = \int_0^c \int_0^a \Phi(\beta_m, x) \cdot \Psi(\gamma_n, y) \cdot \left[v_{ec} \frac{I_{cell}}{\mathcal{V}_{cell}} \left(\frac{\bar{J}}{Y_{ec}} + T_0 \frac{dV_{oc}}{dT} \right) \right.$$
$$\left. + v_{\text{elec},p}\,\dot{g}_{\text{ohm},p} + v_{\text{elec},n}\,\dot{g}_{\text{ohm},n} \right] dx\, dy \qquad [31]$$

and the corresponding integrating constant C must be evaluated from the given initial condition, Eq. (13).

Results and Discussion

In this section, the proposed analytical approach is employed to investigate the thermal behavior of the experimental lithium-ion cell, and the results, i.e. solution of Eq. (29), are compared with experimental temperature measurements and numerical data. The focus of discussions is on the temperature distribution, as electrical aspects (i.e., current and potential distributions) are previously discussed in Refs. 16 and 28.

The analytical solutions, presented in previous section are programmed symbolically in MATHEMATICA (Version 9.0)[32] to obtain a generic solution for the temperature filed. Both analytical and numerical computations are performed on a single processor PC, with a 64-bit quad-core CPU (Core i7) and 10GB of RAM. For analytical

calculations we used built-in functions in MATHEMATICA to find the eigenvalues and to integrate the functions. The presented result are calculated with three terms of series solution in the electrical model [cf. Eq. (24)] and two eigenvalues in each direction of the thermal model [cf. Eq. (29)]. With these conditions the analytical model takes fraction of a minute to complete.

To explain the spatial and temporal temperature behavior in the battery, we compare the evolution of temperature between three different locations during 1C, 2C, and 3C-discharge processes. Results together with the positions of three monitoring points are depicted in Fig. 10. A small convective heat transfer coefficient, $h = 5$ W m^{-2} K^{-1}, is considered at the surfaces and boundaries of the battery; both ambient and initial conditions are set to $T_0 = 22°$C. Temperature of the corresponding locations measured through experimental study (symbols) and calculated by numerical model (dashed-lines) are used to validate the results of the proposed analytical model (lines). Overall, the analytical results are in well consistent with the data acquired from the experiments and numerical simulations. The results in Fig. 10 indicate the occurrence of the maximum temperature at the location 1 which is due to Joule heating caused by the constriction of the current flow at the vicinity of the tab[16,28] as it is confirmed in Fig. 11 presenting the summation of the polarization and ohmic heat generation rates.
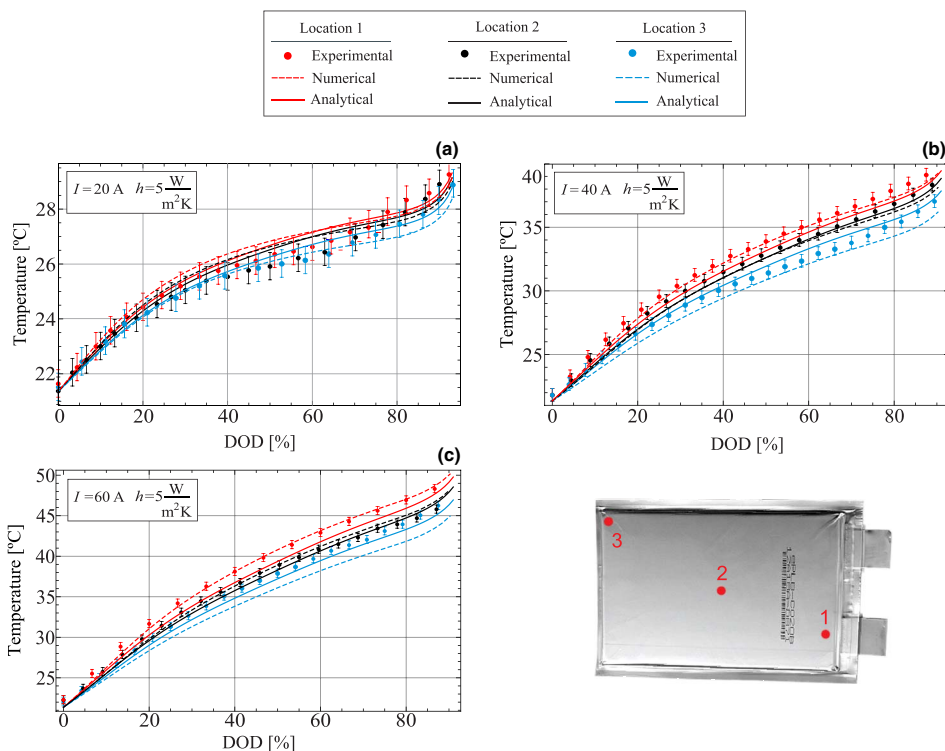

Figure 10. Temperature variation vs. depth of discharge (DOD) is shown for different discharge currents. The maximum temperature at the vicinity of the positive electrode's tab (red lines), the center temperature (black lines), and the minimum temperature at the bottom of the battery (blue lines) are compared with the ones obtained from numerical (dashed lines) and experimental (symbols) studies. A natural convection ($h = 5$ Wm^{-2}K^{-1}) is applied at the surfaces and boundaries of the battery and both ambient and initial temperatures are set to 22°C.
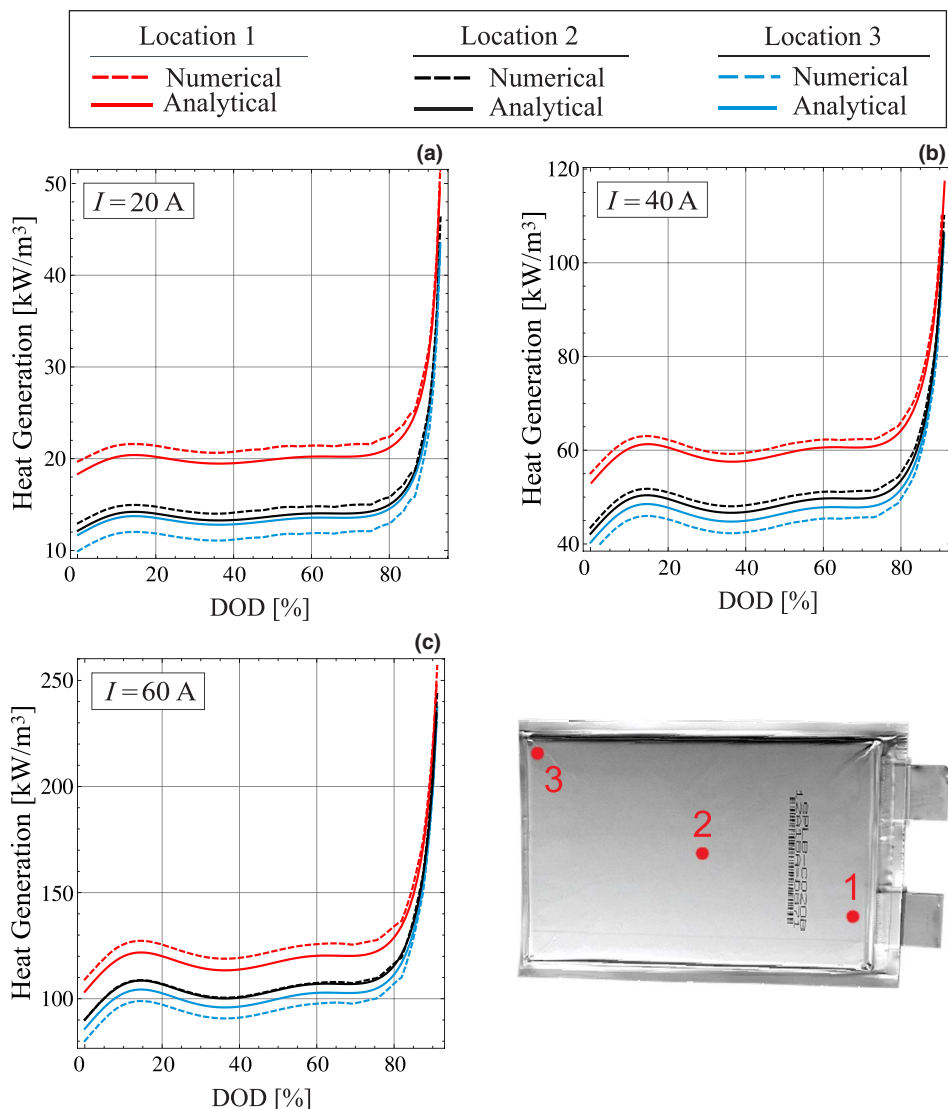
Figure 11. Irreversible heat generation rate (polarization and ohmic heating) vs. depth of discharge (DOD) for different discharge currents calculated at three different locations. The dashed lines represent the numerical data and the solid lines show the ones obtained from Eqs. (26) and (10).

The spatial variation of the volumetric irreversible heat generation rate in the electrode-domain at the end of 1C, 2C, and 3C-discharge processes are plotted in Fig. 12. This quantity over the electrode domain volume includes heat from cell overpotential and ohmic losses obtained from Eqs. (26) and (10). As shown in Fig. 12, the highest rates for heat generation are established on the border of the tabs where the current density is maximum. This increases the temperature in vicinity of the tabs, which in turn accelerates the rate of electro-chemical reactions and promotes the formation of localized hot spots near the tabs.[5] Our calculations for the considered battery show that Joule heating in the electrodes contributes to 8-18% of the total heat generation.

Figure 12 also shows that the heat generation rate in the positive electrode tab is higher than that of the negative electrode tab; the reason is that the current collector of positive electrode which is made by the aluminum foil has larger electrical resistivity than the current
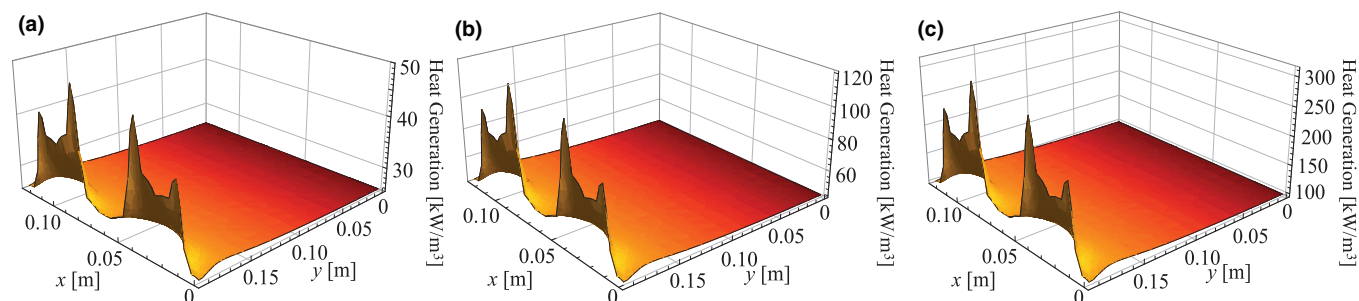

Figure 12. Contour of volumetric irreversible heat generation rate (polarization and ohmic heating) in the cell at the end of a) 1C-discharge process, b) 2C-discharge process, and c) 3C-discharge process.
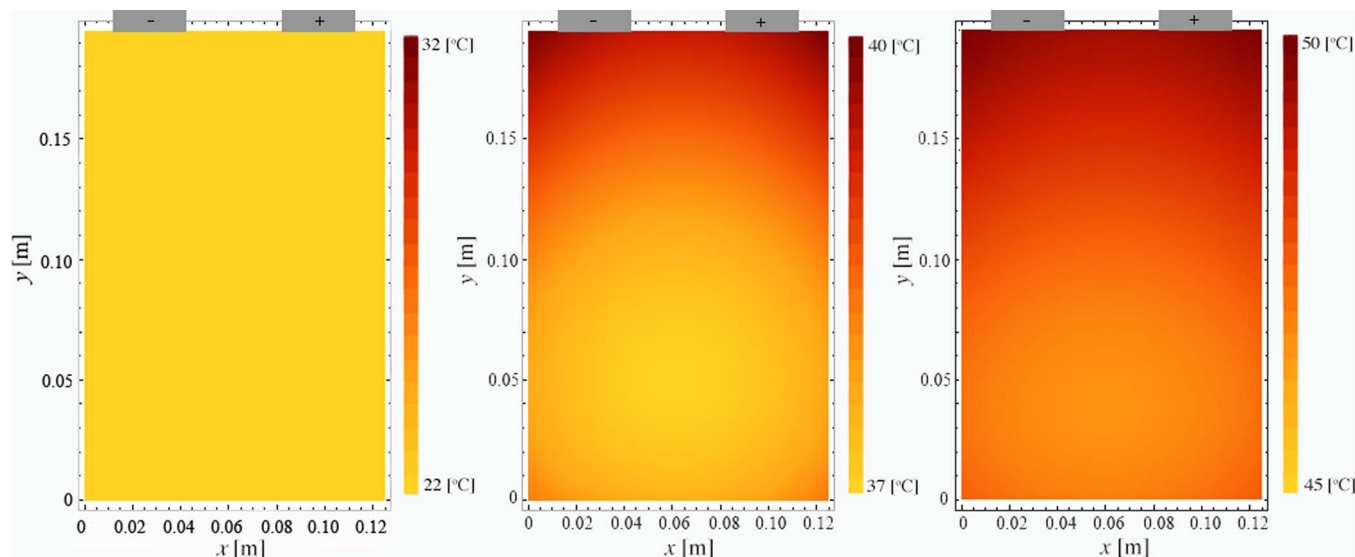
Figure 13. Temperature development within the battery at depth of discharge of a) 0%, b) 50%, c) 90% with a discharge rate of 3C and natural convection ($h = 5 \ \mathrm{W \ m^{-2} \ K^{-1}}$) at the surfaces and boundaries of the battery.

collector of negative electrode which is made by copper foil, and thus more Joulean heat is generated on the positive electrode than on the negative electrode.[17,5,11]

Figure 13 presents the effect of Joulean heat on the battery temperature non-uniformity at a 60 A discharge process. Plots (a)-(c) show the temperature distribution in the electrode domain at three different DOD of 0%, 50%, and 90%, when natural convection ($h = 5 \ W \ m^{-2} \ K^{-1}$) is considered on all the boundaries and surfaces of the battery. As shown in Fig. 13, the spatial temperature imbalance on the cell progressively increases over discharge process. The maximum temperature difference between the hottest and coldest spots of the cell is increased from 3°C at 50% of DOD to 5°C at 90% of DOD which corresponds to the temperature variations presented in Fig. 10 c.

Conclusions

In this study, a new mathematical procedure was performed to accurately predict the ohmic heating and transient temperature behavior of the battery during galvanostatic processes. The following steps were taken to develop and validate the present model:

• a large lithium-ion battery pouch (20 Ah) was characterized experimentally to obtain its polarization expression,
• transient behavior of the battery during constant current discharge processes was simulated numerically to study the distributions of the reaction current density in the electrode assembly,
• based on the constant current density assumption, the governing equations of the electrical model for positive and negative fields were decoupled, an analytical solution was proposed to approximate the ohmic heat generation in the electrode domains. The assumption required for development of the analytical model was justified by an independent full numerical simulation of the problem,
• a compact series form solution for ohmic heating in the battery was obtained and then coupled to the transient thermal model through heat source term,
• the electro-thermal model was solved analytically using method of integral transformation,
• developed model was validated through comparison with the numerical and experimental studies.

It should be emphasized that a uniform transfer current density was assumed in the presented analytical model which is valid for DOD < 90% confirmed by numerical studies.

The validated model was applied to study the transient thermal response of the battery during standard constant current discharge tests. The results showed that the maximum temperature in the battery arises at the vicinity of the tabs, where the ohmic heat is established as a result of the convergence/divergence of the current streamlines. It was confirmed that ohmic heating in the electrode contributes a relatively small portion (8-18%) of the total heat generation in the considered battery; nonetheless, this highly localized heat can cause spatial non-uniformity in total heat generation and consequently in temperature profile.

To conclude, it is important to affirm that the proposed analytical model can be used to study the effect of electrode configurations on the heat generation and temperature profiles. Furthermore, the model may be preferred to a three-dimensional model for investigating the temperature profile on the cross-plane of the battery in which the effect of thermal/electrical contact resistance between the electrodes/separator/current collectors can be taken in to consideration.

List of Symbols

a	width of electrode (m)
b	width of tab (m)
c	height of electrode (m)
c_p	specific heat capacity ($\mathrm{J \ kg^{-1} \ K^{-1}}$)
$\mathscr{C}_l$	interpolation coefficients for Y_{ec}
$\mathscr{C}_T$	temperature coefficient for Y_{ec}
$\mathscr{D}_m$	interpolation coefficients for V_{oc}
$\mathscr{D}_T$	temperature coefficients for V_{oc}
e	distance of tab center from y-axis (m)
$\dot{g}$	heat generation rate ($\mathrm{W \ m^{-3}}$)
$\dot{g}_{ohm}$	ohmic heat generation rate ($\mathrm{W \ m^{-3}}$)
h	heat transfer coefficient ($\mathrm{W \ m^{-2} \ K^{-1}}$)
H	ratio of convective to conduction heat transfer coefficients, h/κ ($\mathrm{m^{-1}}$)
i	in-plane current density ($\mathrm{A \ m^{-2}}$)
I	applied discharge current (A)
J	reaction current density ($\mathrm{A \ m^{-2}}$)

n	unit normal vector on electrode
N	number of cell assemblies inside the battery core
q	in-plane heat flux (W m^{-2})
q_{diss}	heat dissipation flux (W m^{-2})
Q	capacity (A h)
t	time (s)
T	temperature (°C)
T_0	ambient and initial temperature (°C)
T_s	surface temperature (°C)
V	potential (V)
V_{oc}	open-circuit potential (V)
$\mathcal{V}$	volume (m^3)
x	horizontal position (m)
y	vertical position (m)
Y_{ec}	conductance (S m^{-2})

Greek

α_k	k th eigenvalue
β_m	m th eigenvalue in x-direction
γ_n	n th eigenvalue in y-direction
δ	thickness (m)
θ	temperature rise, $T - T_0$ (°C)
κ	thermal conductivity (W m^{-1} K^{-1})
ν	volume ratio
ρ	density of cell assembly (kg m^{-3})
Φ	transformation kernel in x-direction
Ψ	transformation kernel in y-direction
σ	electrical conductivity (S m^{-1})

Subscript

am	related to active material
batt	related to battery
case	related to battery case
cc	related to current collector
cell	related to cell (electrode pair)
ec	related to electrochemical reaction
eff	related to current collector
elec	related to electrode
n	related to the negative domain
p	related to the positive domain
ref	related to the reference temperature
ss	related to separator sheet
x	related to x-direction
y	related to y-direction

Superscript

⁻	averaged value of a property
⁼	transferred quantity based on Eq. (28a)
max	maximum value of a property

References

1. T. M. Bandhauer, S. Garimella, and T. F. Fuller, A critical review of thermal issues in lithium-ion batteries, *J. Electrochem. Soc.*, **158**, R1 (2011).
2. T. M. Bandhauer, S. Garimella, and T. F. Fuller, Temperature-dependent electrochemical heat generation in a commercial lithium-ion battery, *J. Power Sources*, **247**, 618 (2014).
3. J. Yi, U. S. Kim, C. B. Shin, T. Han, and S. Park, Three-dimensional thermal modeling of a lithium-ion battery considering the combined effects of the electrical and thermal contact resistances between current collecting tab and lead wire, *J. Electroche. Soc.*, **160**, A437 (2013).
4. W. Fang, O. J. Kwon, and C. Y. Wang, Electrochemical thermal modeling of automotive li-ion batteries and experimental validation using a three-electrode cell, *Int J. Energ. Res.*, **34**, 107 (2010).
5. G. H. Kim, K. Smith, K. J. Lee, S. Santhanagopalan, and A. Pesaran, Multi-domain modeling of lithium-ion batteries encompassing multi-physics in varied length scales, *J. Electrochem. Soc.*, **158**, A955 (2011).
6. M. Doyle, T. F. Fuller, and J. Newman, Modeling of galvanostatic charge and discharge of the lithium/polymer/insertion cell, *J. Electrochem. Soc.*, **140**, 1526 (1993).
7. M. W. Verbrugge and R. S. Conell, Electrochemical and thermal characterization of battery modules commensurate with electric vehicle integration, *J. Electrochem. Soc.*, **149**, A45 (2002).
8. Y. Hu, S. Yurkovich, Y. Guezennec, and B. J. Yurkovich, Electro-thermal battery model identification for automotive applications, *J. Power Sources*, **196**, 449 (2011).
9. H. Gu, Mathematical analysis of a Zn/NiOOH cell, *J. Electrochem. Soc.*, **130**, 1459 (1983).
10. K. H. Kwon, C. B. Shin, T. H. Kang, and C.-S. Kim, A two-dimensional modeling of a lithium-polymer battery, *J. Power Sources*, **163**, 151 (2006).
11. U. S. Kim, C. B. Shin, and C.-S. Kim, Effect of electrode configuration on the thermal behavior of a lithium-polymer battery, *J. Power Sources*, **180**, 909 (2008).
12. U. S. Kim, C. B. Shin, and C.-S. Kim, Modeling for the scale-up of a lithium-ion polymer battery, *J. Power Sources*, **189**, 841 (2009).
13. U. S. Kim, J. Yi, C. B. Shin, T. Han, and S. Park, Modelling the thermal behavior of a lithium-ion battery during charge, *J. Power Sources*, **196**, 5115 (2011).
14. U. Seong Kim, J. Yi, C. B. Shin, T. Han, and S. Park, Modeling the dependence of the discharge behavior of a lithium-ion battery on the environmental temperature, *J. Electrochem. Soc.*, **158**, A611 (2011).
15. P. Taheri, M. Yazdanpour, and M. Bahrami, Transient three-dimensional thermal model for batteries with thin electrodes, *J. Power Sources*, **243**, 280 (2013).
16. P. Taheri, A. Mansouri, M. Yazdanpour, and M. Bahrami, Theoretical analysis of potential and current distributions in planar electrodes of lithium-ion batteries, *Electrochimica Acta*, **133**, 197 (2014).
17. M. Guo and R. E. White, A distributed thermal model for a li-ion electrode plate pair, *J. Power Sources*, **221**, 334 (2013).
18. J. Newman and W. Tiedemann, Potential and current distribution in electrochemical cells: Interpretation of the half-cell voltage measurements as a function of reference-electrode location, *J. Electrochem. Soc.*, **140**, 1961 (1993).
19. D. R. Baker and M. W. Verbrugge, Temperature and current distribution in thin film batteries, *J. Electrochem. Soc.*, **146**, 2413 (1999).
20. M. Doyle and J. Newman, Analysis of capacity rate data for lithium batteries using simplified models of the discharge process, *J. Appl. Electrochem*, **27**, 846 (1997).
21. D. Bernardi, E. Pawlikowski, and J. Newman, A general energy balance for battery systems, *J. Electrochem. Soc.*, **132**, 5 (1985).
22. Y. Chen and J. W. Evans, Heat transfer phenomena in lithium/polymer electrolyte batteries for electric vehicle application, *J. Electrochem. Soc.*, **140**, 1833 (1993).
23. S. C. Chen, C. C. Wan, and Y. Y. Wang, Thermal analysis of lithium-ion batteries, *J. Power Sources*, **140**, 111 (2005).
24. W. Tiedemann and J. Newman, in: S. Gross, (Ed.), *Battery design, optimization, The Electrochemal Society Proceeding Series*, Pennington, NJ, 39 (1979).
25. R. E. Gerver and J. P. Meyers, Three-dimensional modeling of electrochemical performance and heat generation of lithium-ion batteries in tabbed planar configurations, *J. Electrochem. Soc.*, **158**, A835 (2011).
26. S. Chacko and Y. M. Chung, Thermal modeling of li-ion polymer battery for electric vehicle drive cycles, *J. Power Sources*, **213**, 296 (2012).
27. J. Yi, U. S. Kim, C. B. Shin, T. Han, and S. Park, Modeling the temperature dependence of the discharge behavior of a lithium-ion battery in low environmental temperature, *J. Power Sources*, **244**, 143 (2013).
28. P. Taheri, A. Mansuri, B. S. Schweitzer, M. Yazdanpour, and M. Bahrami, Electrical constriction resistance i current collectors of large-scale lithium-ion batteries, *J. Electrochem. Soc.*, **160**, A1731 (2013).
29. P. Taheri, M. Yazdanpour, and M. Bahrami, A computationally-effective thermal model for spirally wound nickel-metal hydride batteries, *J. Electrochem. Soc.*, **161**, A109 (2014).
30. P. Taheri, M. Yazdanpour, and M. Bahrami, Analytical assessment of the thermal behavior of nickel metal hydride batteries during fast charging, *J. Power Sources*, **245**, 712 (2014).
31. M. N. Özisik, *Boundary value problems of heat conduction*, Dover Publications, New York (1989).
32. I. Wolfram Research, *Mathematica Edition: Version 9.0*, Wolfram Research, Inc., Champaign, Illinois (2012).